Photoacoustics 35 (2024) 100568

Contents lists available at ScienceDirect

Photoacoustics

journal homepage: www.elsevier.com/locate/pacs

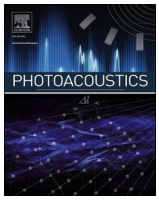

An umbrella-inspired snap-on robotic 3D photoacoustic endoscopic probe for augmented intragastric sensing: Proof of concept study

Li Liu [a], Ang Li [a], Yisong Zhao [a,b], Luyao Zhu [b], Yongjian Zhao [a,*], Fei Gao [b,*]

[a] Department of Electronic Engineering, The Chinese University of Hong Kong, 999077, Hong Kong, special administrative region, China
[b] School of Information Science and Technology, ShanghaiTech University, No. 393 HuaXia Middle Road, Pudong New Dist., 201210, China

ARTICLE INFO

Keywords:
Steerable gastric endoscopy
Three-dimensional photoacoustic tomography
Modular robotic probe
Custom-made ultrasonic array transducer
Early gastric cancer

ABSTRACT

In this paper, we present a novel on-demand modular robotic photoacoustic tomography (PAT) probe integrated into an endoscopic device, potentially for deep intragastric sensing. The proposed solution offers a plug-and-play approach through the use of meso-scale steerable endoscopy and a new 'snap-on' 3D robotic PAT probe that can reconfigure the geometry of the intracorporeal light delivery, inspired by an umbrella structure. Specifically, using the limited esophageal access, steerable endoscopy allows navigation and advancement of a distally mounted robotic add-on for PAT that is folded until it reaches the deep-seated gastric lesion. Once the tip is positioned near the lesion site in the gastric cavity, there is ample working space for the robotic probe to adjust its umbrella-like unfolded shape. This allows fine-tuning of the laser delivery orientation of the fiber bundles to achieve the lesion-specific light delivery scheme. This design allows volumetric imaging of the intragastric PAT with enhanced sensitivity. To evaluate the performance of the modular robotic PAT probe, we performed a simulation analysis of the light intensity and ultrasound field distribution. The simulation results show that the robotic probe is feasible for intracorporeal PAT imaging. In addition, we printed a 3D model of a human stomach containing a simulated gastric tumour. Both the phantom and ex vivo experimental results validate the feasibility of the proposed robotic PAT probe.

1. Introduction

Early gastric cancer (EGC), which is only infiltrated into mucosa or submucosa [1], is a relatively stable biological stage with low incidence of lymph node metastases [1]. The five-year survival rate of EGC has reached 80% after treatment, but early diagnosis rate of EGC is only 5–20% [2]. In clinical practice, the rapid identification of gastric cancer mainly relies on white light endoscopy (WLE) [3,4]. The confirmation of diagnosing suspicious lesions is conducted by selective sample biopsy followed by histological examination. Besides, the treatment plan of gastric cancer is closely related to the tumour invasion depth. However, WLE has limitations in assessing the invasion depth of the gastric tumour [5–7]. Hence, to characterize the lesion deep inside the mucosa, endoscopic ultrasound (EUS) has been introduced to assess the invasion depth for gastric cancer staging [8]. Nevertheless, low EUS image contrast fundamentally limits its ability to exhibit physiologically specific functional information for EGC characterization [9]. Furthermore, macroscopic early-stage gastric tumours are categorized as elevated and flat/depressed types, such that cross-sectional EUS alone cannot be well suited for comprehensive evaluation of tumour morphological variation. These limitations pose a challenge in the identification and characterization of gastric tumours in their early stage. Consequently, it is of urgent necessity to develop a new in situ volumetric imaging modality with excellent contrast, spatial resolution, and penetration depth for determining the shape, volume, and invasion extent of EGC [10].

Photoacoustic Imaging (PAI), an emerging biomedical imaging modality, has developed rapidly and achieved remarkable progress in recent decades [11,12]. PAI holds the merits of both high optical absorption contrast and deep acoustic penetration since it is a hybrid combination of optical and ultrasonic imaging [13,14]. Additionally, it is inherently free of ionization radiation. With these merits, PAI promises to be deployed in various clinical applications according to its system configuration. In general, photoacoustic microscopy (PAM) targets at micro-scale or meso-scale biological tissues where focused laser beam and single element transducer are utilized for PA signal excitation and detection [15,16]. Another configuration is referred to photoacoustic computed tomography (PACT) by using diffused light illumination, multi-channel PA signal acquisition [17,18], and dedicated image

* Corresponding authors.
E-mail addresses: yongjian.1995@link.cuhk.edu.hk (Y. Zhao), gaofei@shanghaitech.edu.cn (F. Gao).

https://doi.org/10.1016/j.pacs.2023.100568
Received 16 July 2023; Received in revised form 1 November 2023; Accepted 3 November 2023
Available online 8 December 2023

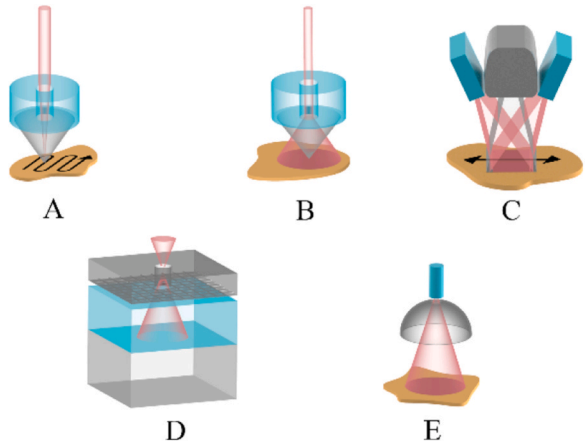

Fig. 1. Representative implementations of 3D PAI system. A. OR-PAM, B. AR-PAM, C. PACT system based on a linear array, and D. PACT system based on a customized 2D array. E. PACT system based on a spherical array.

reconstruction algorithm, which is well suited for macro-scale and deep-seated organ imaging [19]. To yield volumetric PAI, 3D PAM is generally implemented by scanning the focused optical and/or ultrasonic spot in the horizontal plane (Fig. 1.A-B). By contrast, 3D PACT allows for broad light illumination area, and array-based signal detection (Fig. 1.C-E) [20–22]. In term of 3D PAI configuration, the scanning linear array [Fig. 1C] [23], hemispherical array [Fig. 1 E] or full-ring array are usually used in 3D PACT for multichannel sensing [24]. Among them, the scanning in 3D PAM is time-consuming while non-planar transducers associated with 3D PACT may result in coupling problems [25,26].

Conventional paradigms of extracorporeal PAI, such as PACT systems based on clinically available ultrasound probes, face challenges in detecting carcinoma in situ within the gastric lining due to the limited depth of penetration [4,27]. In this context, a promising alternative is the use of endoscopic PAI probes to access the gastrointestinal (GI) tract for intracorporeal imaging and detection [28]. Photoacoustic endoscopy (PAE), a variant of scanning-based PAM, has shown great potential in the detection and diagnosis of early GI cancers. However, it is worth noting that the benefits of PAE are best realized in endoluminal imaging. For applications related to gastrointestinal cross-sections with different diameters, such as intestinal, esophageal, and gastric examinations, a PAE probe with a variable focus is required. To address this challenge, Yang et al. developed an autofocus PAE (AF-PAE), which allows high-resolution imaging of irregular GI tracts, compensating for the loss of lateral resolution caused by the probe's defocus scanning [28]. A major limitation of conventional PAE is the inability to detect in situ tumours in the deep GI tract at depths greater than 5 mm. To address this limitation, Wang et al. proposed a photoacoustic and ultrasound dual-mode endoscopy that can simultaneously image internal organs in vivo [29]. By taking advantage of the complementary strengths of photoacoustic and ultrasound imaging, this integrated PAE/EUS system is expected to be used for the detection and monitoring of deep GI tumours in the clinical setting. In addition, conventional PAE based on single-point scanning protocols may have difficulty in obtaining clear intraluminal high-fidelity PA imaging due to GI peristalsis.

In this paper, we present an on-demand modular robotic photoacoustic tomography (PAT) probe that integrates with a standard endoscopic device at the distal end for potential deep intragastric sensing. This plug-and-play solution combines meso-scale steerable endoscopy with a new 'snap-on' robotic 3D PAT probe inspired by an umbrella structure, enabling reconfigurable intracorporeal light-delivery geometry. In situations where access to the esophagus is limited, the steerable endoscopy system will make it possible for smooth navigation and progression of the folded robotic PAT add-on mounted distally, thus enabling access to deep gastric lesions for enhanced imaging.

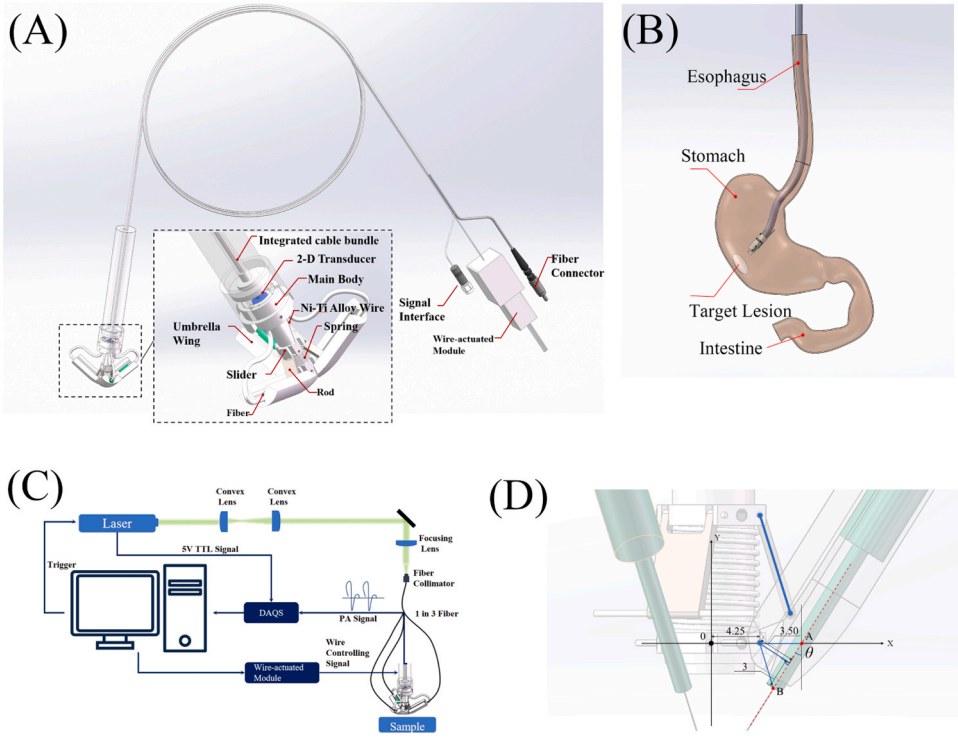

Fig. 2. Schematic diagram illustrating the configuration of the overall system.A. The modular robotic PAT probe design inspired by an umbrella. B. The probe's state of entry into the gastric cavity. C. The endoscopic PAT imaging setup. DAQS: Data Acquisition System; E. The deployment of the robotic probe is described in detail.

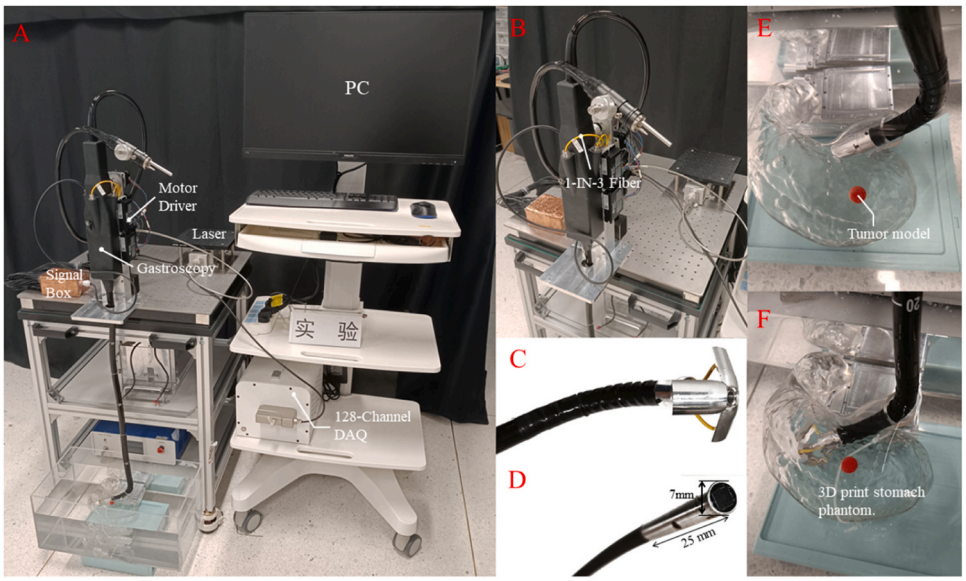

Fig. 3. Overall System and Experimental Setup (A): The setup included a steerable gastric endoscopy system (B), an umbrella-inspired snap-on robotic PAT probe (C), and a custom-made 3D ultrasonic transducer (D). Through the esophagus access, the steerable endoscopy enabled distal mounting of a folded robotic PAT probe towards the simulated tumour (E). Once the endoscopy tip reaches the area near the tumour on the inner stomach wall phantom, a larger intracavity space allows the robotic PAT probe to adjust its umbrella-like unfolded pattern (**F**).

2. Material and methods

2.1. Overall system configuration

Fig. 2-A and B show the overall system configuration that is composed of two components: a modular robotic PAT probe and a meso-system.

2.1.1. Modular robotic PAT probe

The 'snap-on' robotic PAT probe is designed to generate versatile light-delivery configuration for lesion-specific intracorporeal PAT. It is distally interfaced with the gastric endoscopy to facilitate on-demand PAT imaging capability. Such a robotic probe design is inspired by an umbrella-like structure (Fig. 2.A).

2.1.2. Meso-system

The meso-scale gastric endoscopy is used to navigate and steer for delivering an intracorporeal PAT probe into the gastric cavity. Such an endo-cap PAT probe is mounted at the distal end of a conventional gastric endoscopy. Herein, we improve such a passive endoscopy to be active maneuvering, which involves the insertion from the mouth followed by navigation via esophagus access, and ultimately being delivered close to the remote site of the lesion inside the gastric cavity (Fig. 2. B).

2.2. Modular robotic PAT probe

A plug-and-play modular robotic 3D PAT probe was developed and deployed as shown in Fig. 3A. The umbrella-inspired robotic PAT probe is distally interfaced with steerable gastric endoscopy to provide on-demand PAT imaging. The overall robotic add-on comprises two parts: an umbrella-inspired reconfigurable 3D PAT probe and an integrated cable bundle.

2.2.1. Umbrella-inspired re-configurable PAT probe

This probe is composed of a fiber bundle (1-splitting-3), a 2D array transducer, and an umbrella-inspired light-delivery module. The three ferrules at the beam splitter end of the fiber bundle are fixed on the three respective umbrella rib-like structure of the probe, and then the three umbrella ribs are connected to the central axis using three connecting rods. The central axis functions as a hollow cylindrical structure, accommodating a 2D array ultrasonic transducer (Guangzhou Doppler Electronic Technologies Co., Ltd, 7 ×7 =49 elements, pitch: 0.49, array size: 7 mm × 7 mm, central frequency: 5 MHz, bandwidth: 70%, element size: 0.3 mm). A slender wire made of nickel-titanium alloy with a 1 mm diameter passes through the slider and the fixation ring of the connecting rod, ultimately linking to the umbrella rib-like structure. In this setup, the angle of the umbrella rib extension can be adjusted by utilizing an extracorporeal wire-actuated module to push or pull the thin wire, which allows for a lesion-specific, reconfigurable light-delivery system within the stomach.

2.2.2. Integrated cable bundle

To facilitate the transducer signal cable, fiber bundle and actuating push-pull wire to be inserted through the instrument channel of the standard endoscopy, we incorporated them as an integrated cable bundle. The distal end of the integrated cable bundle is connected to the robotic PAT probe via an adaptor while the proximal end is externally connected to the DAQ card (transducer signal cable), laser source (fiber bundle) and wire-actuated module (nickel-titanium alloy wire).

2.3. Meso-system: steerable gastric endoscopy

The meso-system is elaborated in Fig. 2.B. It consists of the proximal control body, insertion tube, and distal bending section. Among them, the distal bending section of the standard gastric endoscopy is modified from manual operation mode to wire-driven control mode. As such, the proximal control body is composed of driving motors and driven wires. The insertion tube provides a wide range of passive motion, whilst the active bending section enables a small-scale range of motion at the distal end of a meso-scale steerable endoscopy. The distal end pose and bending section shape are controlled by pulling and releasing of the silk thread via drive motors. To demonstrate the efficacy of the meso-system, tip position simulations are carried out to assess the workspace and redundancy of the bending section of the endoscopy [30,31]. The study estimates the workspace of the active bending section using the provided parameters of the deployed steerable endoscopy. The details of its workspace and kinematic modeling can be found in the Supplementary

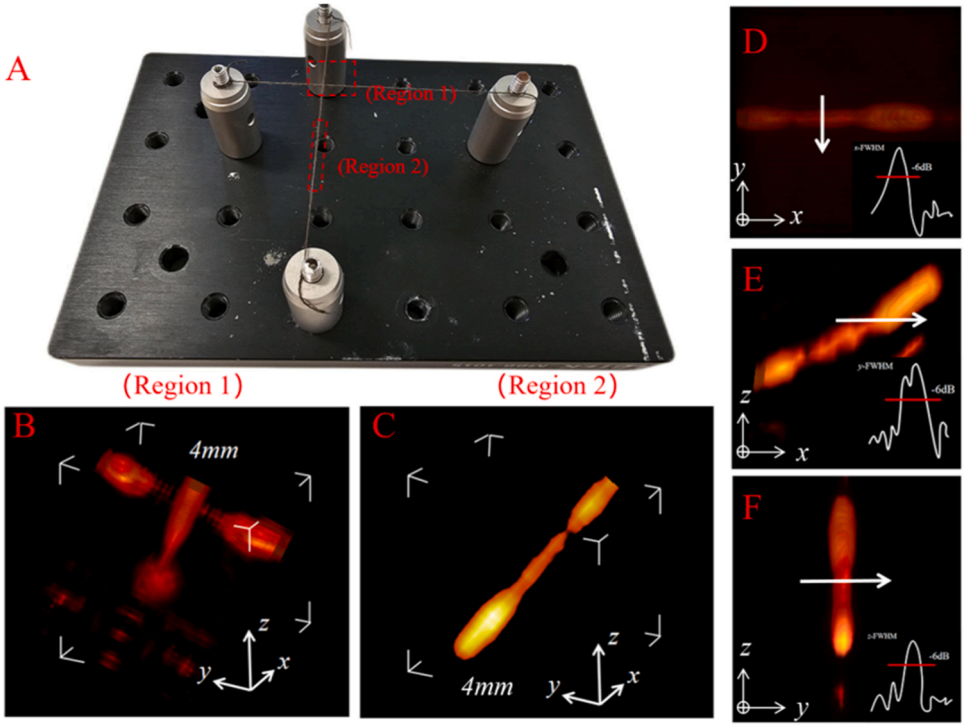

Fig. 4. Phantom experimental results for the characterization of resolution. A. Photograph of the phantom setup. B. PA image of region A. C. PA image of region B. D. *x-y* imaging view of region B and its FWHM. E. *x-z* imaging view of region B and its FWHM. F. *z-y* imaging view of region B and its FWHM.

Materials.

2.4. Optical excitation mode and simulation

In order to fulfill the workspace requirement for deep gastric intracorporeal PAT imaging, the free-space light from the Q-switched pulsed laser is coupled to a fiber bundle, which is divided into three parts, with the end of each attached to the hinge axis of the umbrella-inspired robotic PAT probe, respectively. The incident angle of the laser irradiation onto the target lesion deep-seated within the stomach could be finely tuned by controlling the angle between the hinge axis and the central axis of the modular robotic probe. The pulsed nanosecond light beam from the Q-switched laser (DSC-532–5, CNI) features a 7 ns pulse duration at 532 nm with the pulse energy of 3.3 mJ and a repetition rate up to 20 Hz, which is also an elliptical beam with engery stability is 3% of root mean square (RMS) in energy and 25 μrad in directivity. The laser beam passes through two convex lenses for 3-time beam expansion first, then obtain spatially filtered for better quality of the spot. A pinhole with a diameter of 10 μm is herein located at the posterior focus of the front focusing lens to generate a collimated beam with a diameter of about 6 mm. Afterwards, the combined end of the fiber bundle is placed on a manually adjustable 3D optical rack for fiber position adjustment to maintain the consistency of laser energy yielded by three branches of the fiber. To demonstrate the distribution of light in biological tissues during the adjustment of angles, the propagation of light in biological tissues was simulated using Monte Carlo (MC) method. The MC method was hereby performed using Software Monte Carlo Extreme.

A schematic and the positioning calculation of this simulation is shown in Fig. 2.D Three laser beams with 25.4° divergence angle were simultaneously set in this simulation. The distance between the detector and the surface was set to be 15 mm. A variable θ (see Fig. 2.D) used to control spots distributing on the surface of sample was introduced. Different θ values correspond to different distances between three spots. Four different incident angles were set to get the discrepancies of photon propagation. For the distance of 15 mm, they were 0, $\pi/24$, $\pi/12$, and $\pi/9$, respectively. Besides, in each incident angle of different distances, the photon propagation of cross sections on 4 different depths, and the discrepancies of fluence along the diameter of the circle consisting of three laser beams, were recorded.

All the parameters and scales for this simulation were based on the mechanical design of the detector and sources. For the scattering medium, it was divided into two parts for the simulation of the practical scenario. The part above the surface is water, while the other is the biological tissue. For the biological tissue, the anisotropic factor, refractive index, optical absorption coefficient and optical scattering coefficient of the tissue sample were set to 0.9, 1.37, 0.01 cm^{-1} and 20 cm^{-1}. On the other hand, they were 0.9, 1.37, 2.9×10^{-5} and 1×10^{-6}, respectively for water.

2.5. Experimental setup

As shown in Fig. 2.C, a 5 V TTL (Transistor-Transistor Logic) signal from the laser, which reflects the timing of the laser output, was hereby used to synchronize entire system, including trigger of Data Acquisition System (DAQS). A portable DAQS (Langyuan Inc.) was chosen to collect photoacoustic signals for back-end image reconstruction. The whole acquisition system provides up to 54 dB low-noise signal amplification and up to 12 nV@ 80 dB, 80 MSPS sampling rate and 12-bits resolution. The acquisition mode of the DAQ system was selected as external trigger, that is, the TTL signal of the laser was used to trigger the DAQ system. Besides, the data of the acquired original photoacoustic signal of the array were first averaged to reduce the interference of white noise. At the same time, the Delay and Sum algorithm written in Visual Studio 2019 (Microsoft Inc. US) was used to reconstruct the PA image. To increase the imaging speed, Graphics Processing Units (GeForce RTX 3090, NVIDIA, US) was used to speed up the PAT image reconstruction. Lastly, a frame rate of 15 fps was achieved, which is sufficient to fulfill the intragastric PAT imaging requirements. The photographs of the whole system and details of each component are shown in Fig. 3.

We 3D-printed a human stomach phantom with a simulated gastric tumour extracted from clinical CT data. Through the constrained esophagus access, the steerable endoscopy is actively guided a distally

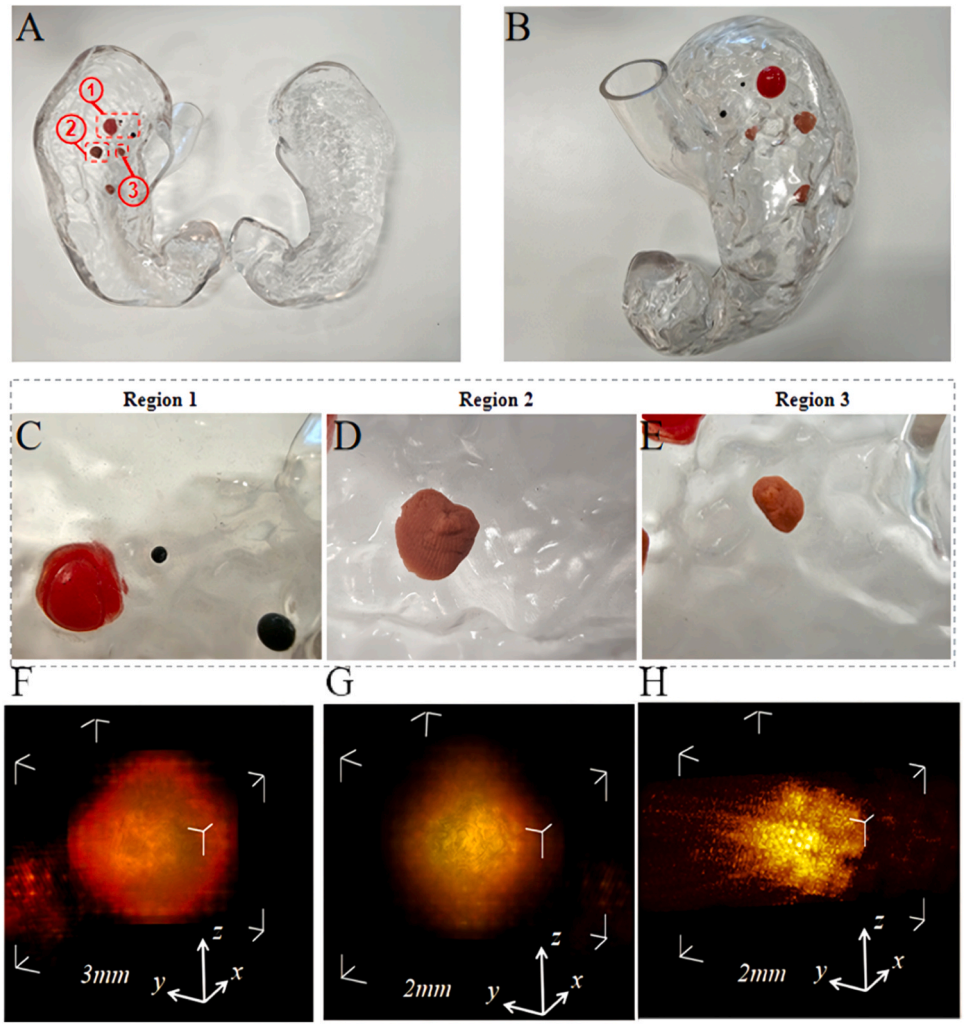

Fig. 5. Photograph of stomach phantom with tumour mock-ups: A. internal view of the phantom, B. external view of the phantom, C.-D.-E. three simulated tumour models on *Region 1*, *Region 2*, and *Region 3*. F.-G.-H. corresponding 3D endoscopic PAT of three simulated tumour models on *Region 1*, *Region 2*, and *Region 3*.

mounted robotic PAT add-on with a folded configuration towards the simulated tumour (Fig. 3.E). Once the tip is delivered close to the tumour site within the gastric cavity, the sufficient workspace can be allowed for the robotic PAT probe to reconfigure its umbrella-like unfolded pattern, such that the lesion-specific light delivery scheme can be achieved by fine tuning the laser irradiation orientation of optic fiber bundles, thereby enabling intragastric PAT volumetric imaging (Fig. 3.F).

3. Phantom experiments

3.1. Cross-wire phantom experiment

We validated our developed endoscopic 3D PAT system using a 2D array transducer on a cross-wire phantom (see Fig. 4.A). The phantom was partitioned into two distinct regions and imaged separately. Specifically, we imaged *Region 1*, made up of intersecting black wires, to confirm the effectiveness of the endoscopic 3D PAT system. We imaged *Region 2*, located below *Region 1*, which consisted of a single black wire, to evaluate the resolution of such an endoscopic PAT system by analyzing PA signals. Since the both cross-wires are not parallel to the horizontal axis, we utilized the geometric projection method to compute the full width at half maximum (FWHM). $\mathrm{FWHM} = 1/\sqrt{1/x - \mathrm{FWHM}^2 + 1/\mathrm{y} - \mathrm{FWHM}^2 + 1/z - \mathrm{FWHM}^2}$, in which x-FWHM, y-FWHM and z-FWHM represent the FWHM values projected on x-axis, y-axis and z-axis, respectively. Using the geometric projection method, the calculation of the full width at half maximum (FWHM) of the wire image yields approximately 0.89 mm. The x-FWHM, y-FWHM, and z-FWHM measurements were 1.75 mm, 1.68 mm, and 1.18 mm, respectively, as shown in Fig. 4.D.-E.-F. Taking into account the actual diameter of the line (0.3 mm), we determined that the reconstructed image had an effective resolution of approximately 0.59 mm. This value is slightly greater than the resolution achieved through K-wave simulation, which was 0.49 mm horizontally and 0.54 mm axially.

3.2. Stomach Phantom Experiment

To simulate various intragastric tumour infiltration models, we created tumour mock-ups of various shapes using Play-Doh as a modeling material (see Fig. 5.A). These simulated tumour targets were attached to the inner surface of the stomach phantom. The entire phantom was submerged in water, and our proposed robotic 3D PAT probe was introduced into the gastric cavity with the aid of a steerable gastric endoscopy. It was used to obtain volumetric PAT images of three distinct target regions featuring tumour models of varying sizes and shapes. C). The first region comprised a dark red infiltrated tumour phantom along with a surrounding black spherical object. The former measured about 2.9 mm in dimension, while the latter had a diameter of 0.5 mm (refer to Fig. 5.**C**). *Region 2* and *Region 3* (refer to Fig. 5.D-E)

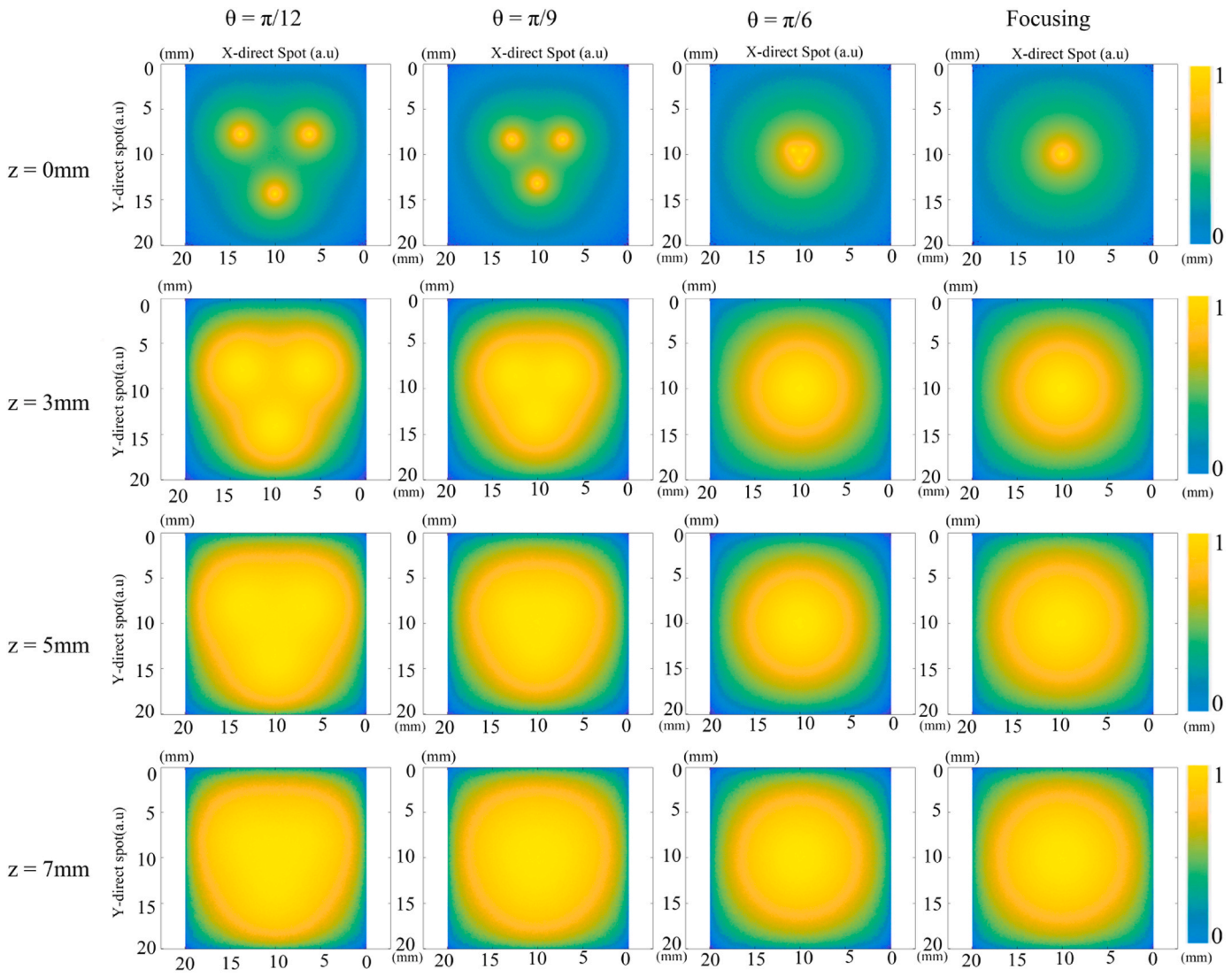

Fig. 6. Monte Carlo simulation results of different light illumination angle in different layers (from 0*mm*–7*mm*). Column A.- D. light distribution on $\theta = \pi/12$, $\pi/9$, $\pi/6$ illumination angles and focusing cases.

consisted of tumour models varying in size and shape, made with Play-Doh and with envelope diameters of 2.1 mm and 1.5 mm, respectively. The 3D PAT images of the simulated tumours are displayed in Fig. 5**.F.-G.-H**, which accurately delineate the tumour models in distinct regions of the stomach phantom.

4. Ex vivo experimental preparation

In order to objectively assess the imaging capabilities of our proposed system on living organisms, we conducted ex vivo experiments on the stomach of a 2-year-old, 128 kg adult pig. The preparation process for the specimen involved creating a small incision with a knife tip in the upper-middle portion of the stomach of a recently slaughtered pig, followed by manual removal of oil.

(1) The preparation process for the specimen involved creating a small incision with a knife tip in the upper-middle portion of the stomach of a recently slaughtered pig, followed by manual removal of oil.
(2) The entire stomach was coated in flour, then rinsed with water to remove any external mucus. Next, the stomach was immersed in warm water for 3 min and removed. The interior was washed out with saline water to dislodge any lingering grease. Our system acquired imaging results without interference from extraneous factors due to our precise specimen preparation.
(3) After initially cleansing and degreasing the samples, we injected approximately 1 mL of ink into two separate regions within the stomach to simulate gastric lesions. To accomplish this, we carefully and obliquely inserted a syringe into the internal mucosa of the stomach and then slowly injected the ink to fully saturate the mucosa. We then covered the opening of the needle with petroleum jelly to prevent any ink leakage. The samples of the injection are depicted in Fig. 9. A and 10. A. To demonstrate the continued reliability of our proposed device in biological imaging, we conducted an experiment wherein a rubber ball with a diameter of 2 mm was embedded beneath the surface of isolated pig stomach tissue(see Fig. 9. A). This deliberate action served the purpose of establishing a contrasting reference point alongside the injected ink area.
(4) Seal the entire stomach with agar and blow continuously through the tube to the stomach inlet to prevent agar from seeping inside and ensure accessibility to the instrument. To obtain an imaged sample sealed within the agar, leave the sample at room temperature (25 °C) for 120 min, the entrance to the stomach remains intact, and the interior space is relatively empty, accurately simulating the environment of the human stomach.

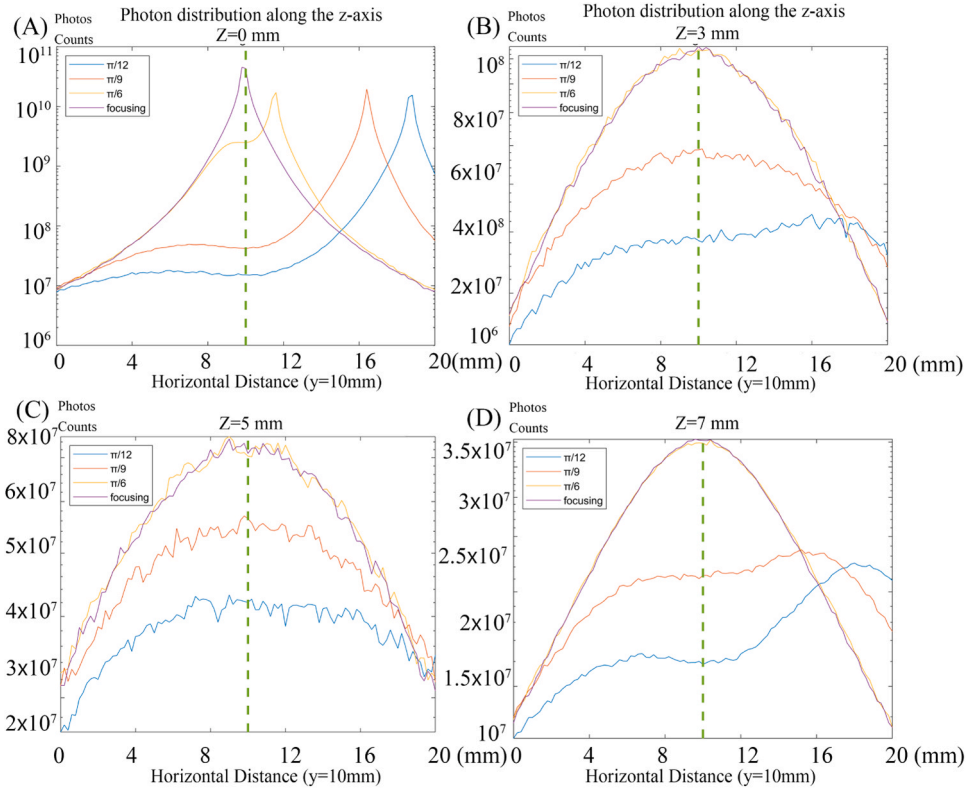

Fig. 7. Light energy distribution along with y = 10 mm in different depths: (A) z = 0 mm. (B) z = 3 mm.(C)z = 5 mm.(D) z = 7 mm.

5. Simulation and ex vivo experimental results

5.1. Optical simulation results

Monte Carlo simulation reveals that for different laser irradiation angles, the illumination pattern on the surface of the sample is not the same with that inside the sample [32]. Columns (A) to (D) in Fig. 6 reflect the illumination distribution of light beams with different incident angles in different depths. It can be clearly observed that the distance between the three beam spots on the surface of the object is the farthest in the case of an illumination angle (refer to Fig. 6.F) of $\pi/24$. As the angle becomes increasingly larger, the three beam spots gradually converge until they completely coincide. Correspondingly, in the dimension of the z-axis, when $\theta = \pi/24$ and $z > 5mm$, the illumination distribution range is larger and more uniform. However, as the three beams converge directly under the image probe, the illumination range gradually increases. Constricted and concentrated, it can provide a higher light intensity. In such a case, a reasonable illumination scheme can be chosen for the sample according to the imaging depth requirements. In order to better characterize the light energy distribution, comparison was conducted between the light spots and different illumination angles at the same z-axis depth horizontally, i.e., each cross-sectional view was drawn at the same z-axis depth along $y =$ 10mm to draw the light energy distribution. The results are shown in Fig. 7.

5.2. Ultrasonic field simulation results

For ultrasonic field simulation, we utilized COMSOL software to simulate the transducer's acoustic pressure distribution. This software is capable of multi-physics field simulation, which visualizes the custom-made device performance and other critical parameters. The Sound Pressure Level (SPL) distribution of paraxial area and spherical area of 2D ultrasound array was calculated, together with a directivity index image. Within the paraxial area, a high SPL level is achieved at about 75 dB (a 1 V voltage is exerted on the transducers), which exceeds the SPL outside the main beam by 6 dB. Fig. 8.A describes the paraxial acoustic sensitivity, while Fig. 8.B shows the spherical acoustic sensitivity distribution of the array. The acoustic sensitivity distribution of X-Y cross section ($z = 10mm$) was also calculated, as shown in Fig. 8. C. While working at a frequency of 100 kHz, this transducer array has a main beam within 71° (Fig. 8.D depicts the array's far-field directivity index), and two sidelobes at about ± 50°. Fig. 8.E shows the far-field Directivity Index (DI) of the array transducer from 50 kHz to 200 kHz. Overall, this array transducer could achieve a superior directivity, acoustic sensitivity and homogeneity within its main beam area (when $z < 5mm$), and the maximum difference of the acoustic sensitivity was estimated to be within 7 dB.

5.3. 3D endoscopic PAT results of ex vivo porcine stomach

Fig. 9 3D endoscopic PAT results of two injection area 1 of the ex vivo porcine stomach.A. tisssue with ink inject at area 1 B. ISO view of 3D PAT. C. *x-z* plane view of 3D PAT. D. *y-z* plane view of 3D PAT. E. *y-x* plane view of 3D PAT.

3D PA imaging results of reference image and two injection areas in a volumetric rendered view are illustrated in Fig. 9.A,10.A,11.A. and its 2D maximum amplitude projections (MAP) are given in Fig. 9.B.-C.-D, 10.B.-C.-D, 11.B.-C.-D and F.-G.-H. The lateral resolution is measured using line spread function (LSF), which, at the depth of 6 mm and 9 mm, is estimated to be about 0.67 mm and 0.82 mm, respectively. Similarly, axial resolution is also estimated at 0.76 mm. Contrast-to-noise ratio (CNR) of the captured PA image is calculated by $\boldsymbol{CNR} = 20\log\frac{|\overline{S}_i - \overline{S}_b|}{\sqrt{\sigma_b^2}}$, where $\overline{S}_i$ is the mean brightness value of the imaging target that is manually selected within a 10-voxel line inside the tumour image, $\overline{S}_b$ and σ_b^2 represent the mean brightness value and the variance of the brightness value of the background within a $5 \times 5 \times 5$-voxel cube

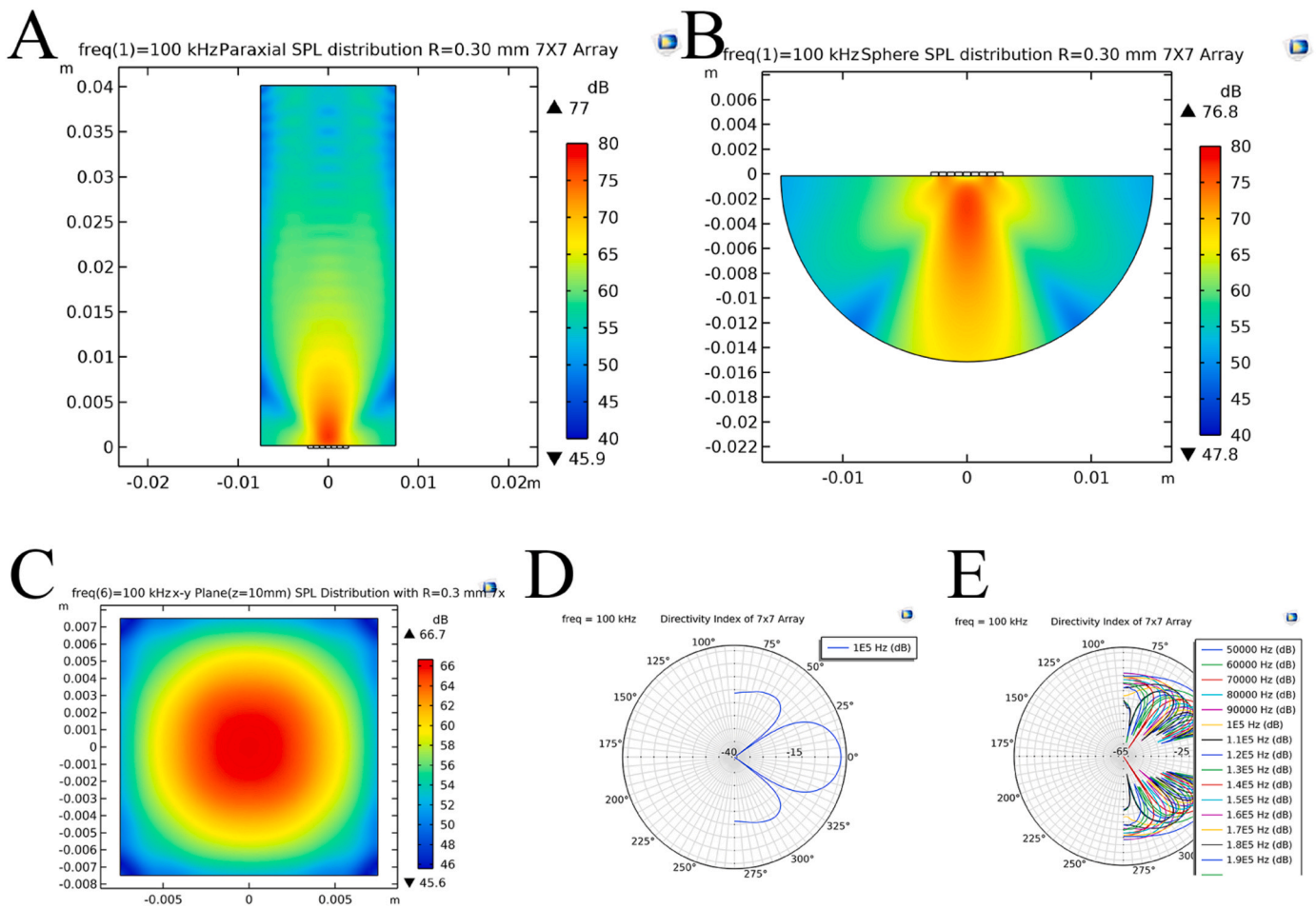

Fig. 8. Ultrasonic field simulation results. A. Paraxial Sound Pressure Level (SPL) distribution. B. Spherical SPL distribution. C. SPL distribution at x-z plane at 100 kHz, z = 10 mm. D. Far-field Directivity Index (DI) of the array @ 100 kHz. E. Far-field Directivity Index (DI) of the array from 50 kHz to 200 kHz.

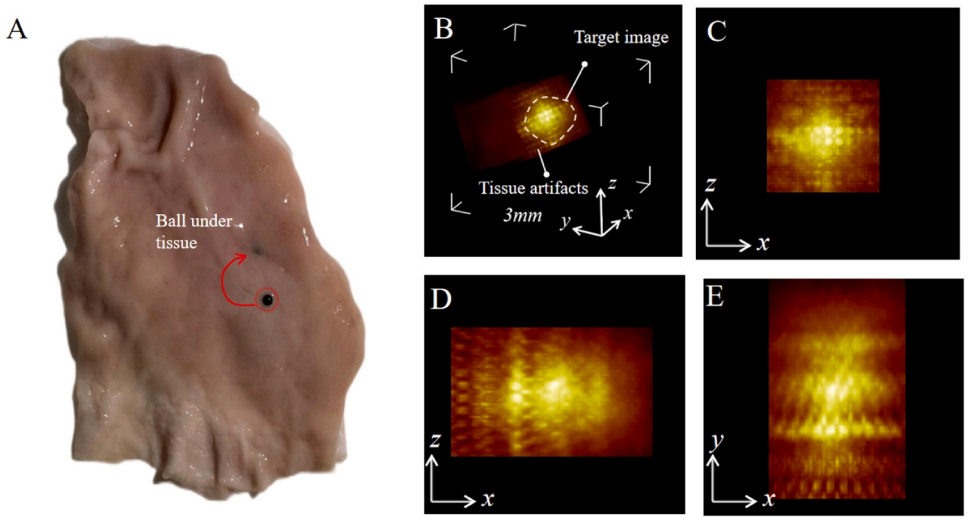

Fig. 9. 3D endoscopic PAT imaging results of rubber ball(reference imaging). A. ex-vivo tissue with ball buried in. B. ISO view of 3D PAT image. C. x-z plane view of 3D PAT image. D. y-z plane view of 3D PAT image. E. y-x plane view of 3D PAT image.

outside the phantom image. In this way, image CNR is calculated to be about 16.3 dB [16.1 ± 0.2 dB (mean standard deviation) at 11 mm in depth,19.6 ± 0.2 dB at 14 mm]. Sidelobe level, calculated by dividing the mean brightness value of the imaging sidelobe by the mean brightness value of the phantom image, is calculated to be −10.4 dB ± 0.5 dB.

6. Discussion

Our proposed probe has been evaluated by imaging a cross-wire model and analyzing the signal, achieving an effective resolution of approximately 0.74 mm. We also assessed the system's ability to detect

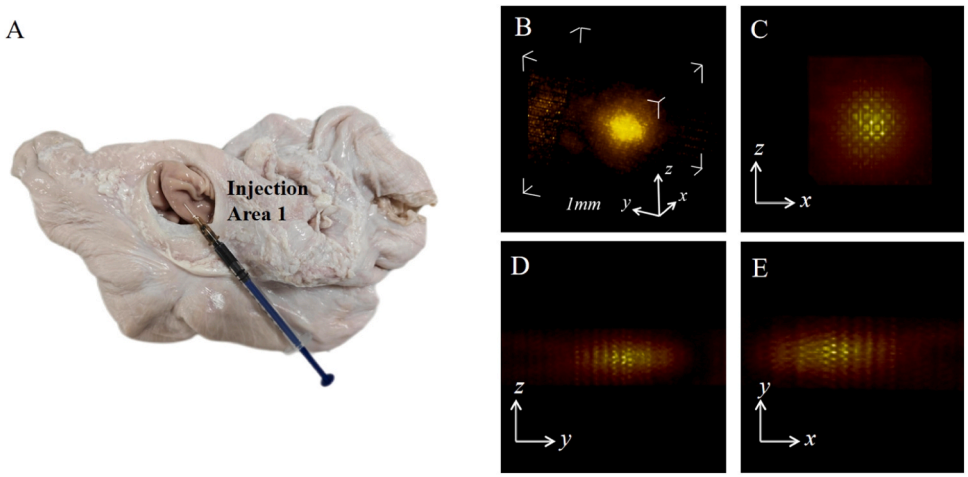

Fig. 10. 3D endoscopic PAT results of two injection area 2 of the ex vivo porcine stomach.A. tisssue with ink inject at area 1 B. ISO view of 3D PAT. C. *x-z* plane view of 3D PAT. D. *y-z* plane view of 3D PAT. E. *y-x* plane view of 3D PAT.

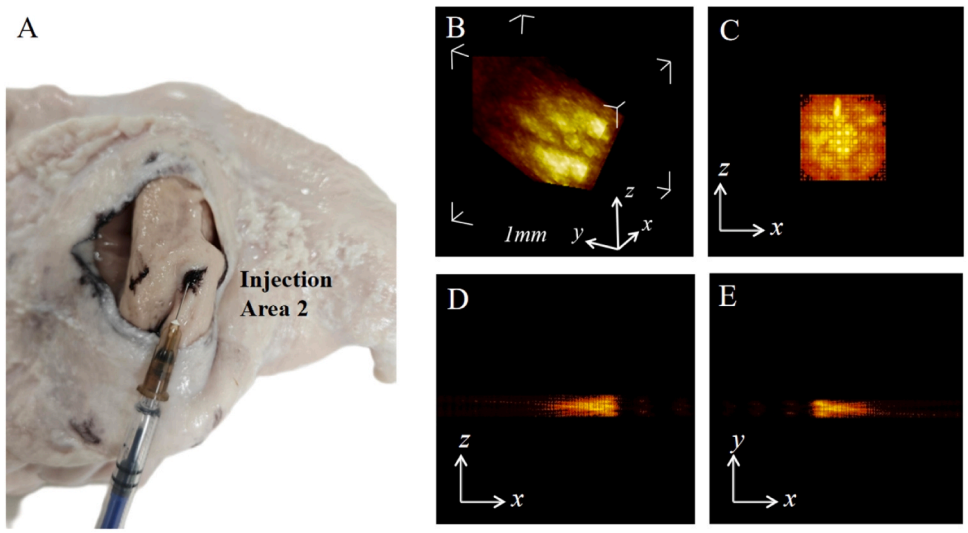

Fig. 11. 3D endoscopic PAT results of two injection area 2 of the *ex vivo* porcine stomach.A. tisssue with ink inject at area 1 B. ISO view of 3D PAT. C. *x-z* plane view of 3D PAT. D. *y-z* plane view of 3D PAT. E. *y-x* plane view of 3D PAT.

invasive tumours in the stomach with model clays and rubber spheres simulating tumours of varying shapes. The imaging results demonstrated the system's ability to proficiently distinguish between tumours of varying shapes. To further verify the system's performance, ex vivo experiments were conducted using sealed agar porcine stomach samples. Black ink was injected into the samples prior to 3D imaging to emulate diseased tissue. The resulting images were analyzed to determine the system's contrast imaging characterization across different areas of the stomach.

Compared to existing endoscopic imaging techniques such as WLE, EUS and scanning-based PAE, our proposed endoscopic PAT device has several advantages: 1) It enables deeper penetration than WLE, which can only show superficial tissue appearance. It can also provide molecular/functional information about the tumour by using multi-wavelength laser, such as oxygenation, compared to EUS, which can only show anatomical information; 2) It provides real-time volumetric PAT imaging based on miniature 2D array sensors yielding greater field of view (FoV) and faster imaging speed than traditional scanning-based PAE. The conventional scanning-based PAE method for detecting GI cancer is limited in terms of real-time capability and clinically relevant large FOV. In contrast, PACT provides an alternative due to its high temporal resolution, extensive penetration depth, and broad FOV. For detecting gastric cancer, high temporal resolution and a wide field of view are essential factors.

The biocompatibility of a robotic intracorporeal PAT probe must be assessed. Validation of the system's safety requires clinical trials that pass safety and ethical reviews, and ensure the system has real-time energy monitoring feedback to guarantee experiment safety and accuracy. Future clinical studies will include these experiments. We present the various light patterns at different illumination angles in Fig. 6. It is assumed that the conventional PAT probe design (fixed at one of the angles) was used. To make an equitable comparison, we must also account for probe setups that lack an umbrella structure and install fiber optic bundles near the array transducer. According to experimental analysis, coaxial photoacoustic coupling is not required to attain optimal imaging depth. In addition, lateral illumination allows for a more accurate characterization of the target object's profile, which is essential for this study. Therefore, we will explore alternative approaches of coaxial photoacoustic imaging in future study.

Another crucial safety concern is the potential injury caused by the metal contacts inside the stomach after the umbrella-shaped robotic probe is deployed. These contacts can scratch the gastric mucosa and

lead to bleeding. To address this issue, we propose two potential solutions, which will be incorporated in our future optimizations. The first solution involves modifying the front probe design, using medical-grade biocompatible plastic and incorporating rounded edges to prevent sharp corners. Secondly, we plan to integrate a compact distance sensor into the umbrella design to avoid collisions with the abdominal wall upon deployment, therefore minimizing any potential safety hazards.

Furthermore, the assessment of gastric lesions necessitates a consideration of the continuous physiological peristalsis that occurs within the gastric organs. This dynamic character of gastric tumors highlights the need for an imaging frame rate of 15 fps, which adequately addresses the issue of image misalignment. Nevertheless, there is still ample room for enhancement. Therefore, in this case, the issue can be resolved by enhancing the imaging rate with a laser source that has a higher repetition rate and by controlling the robotic steerable endoscopy for real-time tracking to ensure the target tumour is within the appropriate region for imaging. In future studies, we will further investigate a robotic visual servoing strategy in dynamic settings to attain superior 3D PAT imaging.

7. Conclusion

In this article, we present a modular robotic endoscopic probe capable of PAT, designed and fabricated to interface distally with a steerable gastric endoscopy. The overall system is compact and easy to use. To enable comprehensive in situ assessment of gastric tumours, the imaging probe can automatically fold through a narrow esophageal passage, allowing for precise and safe delivery of the PAT probe to the designated detection area upon request. On this basis, we performed kinematic modeling of a steerable endoscopy with a modified wire-driven mechanism and estimated the workspace. According to our findings, the robot can cover the entire size of an adult stomach, indicating that the imaging system's distal end can fulfill the detection needs of a variety of lesions in the stomach. After insertion into the stomach, the fiber-optic support units, comprising three extension arms, can perform laser irradiation from varying angles using a wire-driven mechanism. The light illuminating scheme can effectively adapt to a diverse range of samples, encompassing bright field, dark field, and reconfigurable hybrid field. Monte Carlo simulations are utilized to determine light distribution and the corresponding illumination range for the different schemes. Additionally, we have miniaturized the system using customized planar array ultrasound sensors for 3D real-time PAT imaging.

Funding

This work was supported in part by the National Key R&D Program of China under Grant 2019YFB1312400, in part by the Hong Kong RGC TRS under Grant T42–409/18-R, and in part by the Hong Kong RGC GRF under Grant 14204321 and 14211420, GRF under 14220622.

Declaration of Competing Interest

The authors declare that they have no known competing financial interests or personal relationships that could have appeared to influence the work reported in this paper.

Data availability

No data was used for the research described in the article.

Appendix A. Supporting information

Supplementary data associated with this article can be found in the online version at doi:10.1016/j.pacs.2023.100568.

References

[1] S.M. Everett, A.T.R. Axon, Early gastric cancer in Europe, Gut 41 (1997) 142.
[2] Y.K. Tan, J.W.L. Fielding, Early diagnosis of early gastric cancer, Eur. J. Gastroenterol. Hepatol. (18) (2006).
[3] T. Gotoda, Endoscopic resection of early gastric cancer, Gastric Cancer 10 (2007) 1–11.
[4] K. Yao, G.K. Anagnostopoulos, K. Ragunath, Magnifying endoscopy for diagnosing and delineating early gastric cancer, Endoscopy 41 (2009) 462–467.
[5] F. Habib, B. Jobe, Nov. Diagn. Technol. (2019) 141–156.
[6] M. Kim, et al., Intra-instrument channel workable, optical-resolution photoacoustic and ultrasonic mini-probe system for gastrointestinal endoscopy, Photoacoustics 26 (2022), 100346.
[7] S.H. Kim, S.J. Hong, Current status of image-enhanced endoscopy for early identification of esophageal neoplasms, Clin. Endosc. 54 (2021) 464–476.
[8] H. Tsukuma, A. Oshima, H. Narahara, T. Morii, Natural history of early gastric cancer: a non-concurrent, long term, follow up study, Gut 47 (2000) 618–621.
[9] D.T. Schmitt, P.C. Ivanov, Fractal scale-invariant and nonlinear properties of cardiac dynamics remain stable with advanced age: a new mechanistic picture of cardiac control in healthy elderly, Am. J. Physiol. Regul. Integr. Comp. Physiol. 293 (2007) R1923–R1937.
[10] K. Akahoshi, et al., Preoperative evaluation of gastric cancer by endoscopic ultrasound, Gut 32 (1991) 479–482.
[11] P. Beard, Biomedical photoacoustic imaging, Interface Focus 1 (2011) 602–631.
[12] H.F. Zhang, K. Maslov, G. Stoica, L.V. Wang, Functional photoacoustic microscopy for high-resolution and noninvasive in vivo imaging, Nat. Biotechnol. 24 (2006) 848–851.
[13] O. Jung-Taek, L. Meng-Lin, F.Z. Hao, M. Konstantin, V.W. Lihong, Three-dimensional imaging of skin melanoma in vivo by dual-wavelength photoacoustic microscopy, J. Biomed. Opt. 11 (2006), 034032.
[14] P. Manojit, V.W. Lihong, Thermoacoustic and photoacoustic sensing of temperature, J. Biomed. Opt. 14 (2009), 054024.
[15] H. Guo, Y. Li, W. Qi, L. Xi, Photoacoustic endoscopy: a progress review, J. Biophotonics 13 (2020), e202000217.
[16] J. Yao, L.V. Wang, Photoacoustic microscopy, Laser Photon Rev. 7 (2013).
[17] S.E. Bohndiek, et al., Photoacoustic tomography detects early vessel regression and normalization during ovarian tumor response to the antiangiogenic therapy trebananib, J. Nucl. Med. 56 (2015) 1942.
[18] Y. Zhao, et al., A light-adjustable hand-held probe for photoacoustic tomography in vivo, IEEE J. Sel. Top. Quantum Electron. 27 (2021) 1–11.
[19] P. Hajireza, W. Shi, R.J. Zemp, Real-time handheld optical-resolution photoacoustic microscopy, Opt. Express 19 (2011) 20097–20102.
[20] M. Nasiriavanaki, et al., High-resolution photoacoustic tomography of resting-state functional connectivity in the mouse brain, Proc. Natl. Acad. Sci. 111 (2014) 21–26.
[21] S. Liang, I.M. Konstantin, B. Rachel, K.K. Shung, V.W. Lihong, Fast 3-D dark-field reflection-mode photoacoustic microscopy in vivo with a 30-MHz ultrasound linear array, J. Biomed. Opt. 13 (2008), 054028.
[22] X. Wang, Y. Pang, G. Ku, G. Stoica, L.V. Wang, Three-dimensional laser-induced photoacoustic tomography of mouse brain with the skin and skull intact, Opt. Lett. 28 (2003) 1739–1741.
[23] S. Liu, et al., Handheld photoacoustic imager for theranostics in 3D, IEEE Trans. Med. Imaging 38 (2019) 2037–2046.
[24] S. Vaithilingam, et al., Three-dimensional photoacoustic imaging using a two-dimensional CMUT array, IEEE Trans. Ultrason. Ferroelectr. Freq. Control 56 (2009) 2411–2419.
[25] J.Z. Roger, et al., Photoacoustic imaging of the microvasculature with a high-frequency ultrasound array transducer, J. Biomed. Opt. 12 (2007), 010501.
[26] Y. Tan, K. Xia, Q. Ren, C. Li, Three-dimensional photoacoustic imaging via scanning a one dimensional linear unfocused ultrasound array, Opt. Express 25 (2017) 8022–8028.
[27] U. Plöckinger, Diagnosis and treatment of gastric neuroendocrine tumours, Wien. Klin. Wochenschr. 119 (2007) 570–572.
[28] K. Xiong, S. Yang, X. Li, D. Xing, Autofocusing optical-resolution photoacoustic endoscopy, Opt. Lett. 43 (2018) 1846–1849.
[29] J.-M. Yang, et al., Simultaneous functional photoacoustic and ultrasonic endoscopy of internal organs in vivo, Nat. Med. 18 (2012) 1297–1302.
[30] I.D. Walker, C. Carreras, R. McDonnell, G. Grimes, Extension versus bending for continuum robots, Int. J. Adv. Robot. Syst. 3 (2006) 26.
[31] W. McMahan B.A. Jones I.D. Walker Design and implementation of a multi-section continuum robot: Air-octor IEEE/RSJ Int. Conf. Intell. Robots Syst. 2005 2578 2585.
[32] Q. Fang, D.A. Boas, Monte Carlo simulation of photon migration in 3D turbid media accelerated by graphics processing units, Opt. Express 17 (2009) 20178–20190.

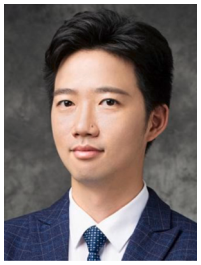

Li Liu : LIU Li received his Ph.D. degree in Biomedical Engineering from the University of Bern, Switzerland, and then worked as a postdoctoral fellow at the University of Bern and the Chinese. University of Hong Kong. He held the position of assistant professor in the School of Biomedical. Engineering at Shenzhen University since 2016. In 2019 he joined CUHK as a faculty member. He has served as Program and Publication Chair of many international conferences including. Publication Chair of IEEE ICIA 2017, 2018 and Program Chair of ROBIO 2019, Video Chair of. IEEE ICRA 2021. He served as Associate Editor of Biomimetic Intelligence and Robotics (BIROB) since 2021. He is a recipient of the Distinguished Doctorate Dissertation Award, Swiss Institute of Computer Assisted Surgery (2016), the MICCAI Student Travel Award (2014) and the Best Paper Award of IEEE ICIA (2009).

Ang Li: Mr.Li received his bachelor degree in M.E from Northeast University, and Master degree Now he is purchasing his ph.D. degree in The Chinese University of Hong Kong (CUHK). His interests includes Biomedical image processing.

Yisong Zhao: A graduate of Sorbonne University with a degree in Electrical Engineering. Currently, he is a Research Assistant and prospective Ph.D. candidate at the Faculty of Engineering, The Chinese University of Hong Kong. His research focus lies in the domains of continuous robotics control and optimization control. His academic journey and hands-on experience have equipped him with a strong foundation in these areas. He is committed to advancing the field through rigorous research and contributing valuable insights to the scientific community.

Luyao Zhu : Miss. Zhu earned his bachelor's degree in computer science from ShanghaiTech University in 2021. Now she is purchasing his master degree in ShanghaiTech University. Her interests includes clinical application on photoacoustic imaging.

Yongjian Zhao: Mr.Zhao received his bachelor degree in M.E from Anhui University of. Technology in 2018, and Master degree in Electrical and Electronic Engineering from University of Chinese Academy of Sciences in 2021. Now he is purchasing his ph.D. degree in The Chinese. University of Hong Kong (CUHK). His interests includes Surgical Robots and its navigation.

Fei Gao: Dr. Gao received his bachelor degree in Microelectronics from Xi'an JiaoTong University in 2009, and PhD degree in Electrical and Electronic Engineering from Nanyang Technological University, Singapore in 2015. He joined School of Information Science and Technology, ShanghaiTech University as an assistant professor in Jan. 2017, and established Hybrid Imaging System Laboratory (HISLab: www.hislab.cn). During his PhD study, he has received Chinese Government Award for Outstanding Self-Financed Students Abroad (2014). His PhD thesis was selected as Springer Thesis Award 2016. He is currently serving as editorial board member of Photoacoustics. He has published about 130 journal and conference papers with 2000 + citations. His interdisciplinary research topics include photoacoustic (PA) imaging physics (proposed passive PA effect, PA resonance imaging, phase-domain PA sensing, pulsed-CW hybrid nonlinear PA imaging, TRPA-TRUE focusing inside scattering medium, etc.), biomedical circuits and systems (proposed miniaturization methods of laser source and ultrasound sensors, delay-line based DAQ system, hardware acceleration for PA imaging, etc.), algorithm and AI (proposed frameworks such as Ki-GAN, AS-Net, Y-Net, EDA-Net, DR2U-Net, etc,), as well as close collaboration with doctors to address unmet clinical needs (Some prototypes are under clinical trials).